Eur. Phys. J. A (2011) **47**: 50
DOI 10.1140/epja/i2011-11050-3

THE EUROPEAN PHYSICAL JOURNAL A

Regular Article – Experimental Physics

Elastic and inelastic scattering of $^{14}C + ^{18}O$ versus $^{12,13}C + ^{18}O$ and $^{14}C + ^{16}O$

A.T. Rudchik[1,a], Yu.O. Shyrma[1], K.W. Kemper[2], K. Rusek[3], E.I. Koshchy[4], S. Kliczewski[5], B.G. Novatsky[6], O.A. Ponkratenko[1], E. Piasecki[7], G.P. Romanyshyna[1], Yu.M. Stepanenko[1], I. Strojek[3], S.B. Sakuta[6], A. Budzanowski[5], L. Głowacka[8], I. Skwirczyńska[5], R. Siudak[5], J. Choiński[7], and A. Szczurek[5]

[1] Institute for Nuclear Research, Prospekt Nauky 47, 03680 Kyiv, Ukraine
[2] Physics Department, Florida State University, Tallahassee, FL 32306-4350, USA
[3] A. Soltan Institute for Nuclear Studies, ul. Hoża 69, PL-00-681 Warsaw, Poland
[4] Kharkiv National University, pl. Svobody 4, 61077 Kharkiv, Ukraine
[5] H. Niewodniczański Institute of Nuclear Physics, ul. Radzikowskiego 152, PL-31-342 Cracow, Poland
[6] Russian Research Center "Kurchatov Institute", Kurchatov Sq. 1, 123182 Moscow, Russia
[7] Heavy Ion Laboratory of Warsaw University, ul. L. Pasteura 5A, PL-02-093 Warsaw, Poland
[8] Institute of Applied Physics, MUT, ul. Kaliskiego 2, PL-00-908 Warsaw, Poland

Received: 19 December 2010 / Revised: 18 March 2011
Published online: 20 April 2011

Communicated by A.A. Korsheninnikov

Abstract. The angular distributions of the $^{14}C + ^{18}O$ elastic and inelastic scattering at the energy $E_{lab}(^{18}O) = 105\,MeV$ were measured firstly. The data were analyzed within the optical model and the coupled-reaction-channels method. The parameters of the $^{14}C + ^{18}O$ optical potential were deduced. The contributions of one- and two-step transfers of nucleons and clusters in the $^{14}C + ^{18}O$ elastic and inelastic scattering were calculated. The isotopic differences between the $^{14}C + ^{18}O$ and $^{12,13,14}C + ^{18}O$ potentials were studied.

1 Introduction

Recently the isotopic differences between the elastic scattering of $^{12}C + ^{16}O$ and $^{12}C + ^{18}O$, $^{12}C + ^{18}O$ and $^{13}C + ^{18}O$, and $^{13}C + ^{16}O$ and $^{13}C + ^{18}O$ have been studied over a wide energy range within the coupled-reaction-channels (CRC) method (see refs. [1,2] and references there). It was found that the transfer reaction contributions to the large-angle scattering of $^{12}C + ^{16}O$ and $^{12}C + ^{18}O$ differ significantly and that the $^{12}C + ^{16,18}O$ potentials have similar real potentials, but differ in their imaginary parts at large separation distances. Similar results were also observed in the $^{12,13}C + ^{18}O$ and $^{13}C + ^{16,18}O$ elastic-scattering studies.

In the present work, we continue the study of isotopic effects in carbon scattering from oxygen by reporting the results for angular distributions of the $^{14}C + ^{18}O$ elastic and inelastic scattering measured at the energy $E_{lab}(^{18}O) = 105\,MeV$. To our knowledge, this is the first data set reported for this system. Previously, the angular distributions of the $^{12,13}C + ^{18}O$ elastic and inelastic scattering were measured also at this energy. With these new measurements, it was possible to carry out a comparative study of scattering in the systems $^{12,13,14}C + ^{18}O$ and $^{14}C + ^{16,18}O$ which is reported in the present work.

The paper is organized as follows. Section 2 is a short description of the experimental procedure. Results of the $^{14}C + ^{18}O$ elastic- and inelastic-scattering data analysis and the $^{12,13,14}C + ^{18}O$ and $^{14}C + ^{16,18}O$ isotopic effects are given in sect. 3. The summary and conclusions can be found in sect. 4.

2 Experimental procedure

Angular distributions for the $^{14}C(^{18}O, X)$ reactions were measured at the energy $E_{lab}(^{18}O) = 105\,MeV$ using a ^{18}O beam from the Warsaw University cyclotron C-200P. The beam energy spread on the target was about 0.5%. A self-supporting $280\,\mu g/cm^2$ foil of carbon enriched upto 86% in ^{14}C was used as a target.

The experimental details are presented in ref. [1]. A typical $\Delta E(E)$-spectrum measured with a telescope composed of a $67\,\mu m$ ΔE detector is presented in fig. 1, where the intensity of the different particle groups shows the

[a] e-mail: rudchik@kinr.kiev.ua

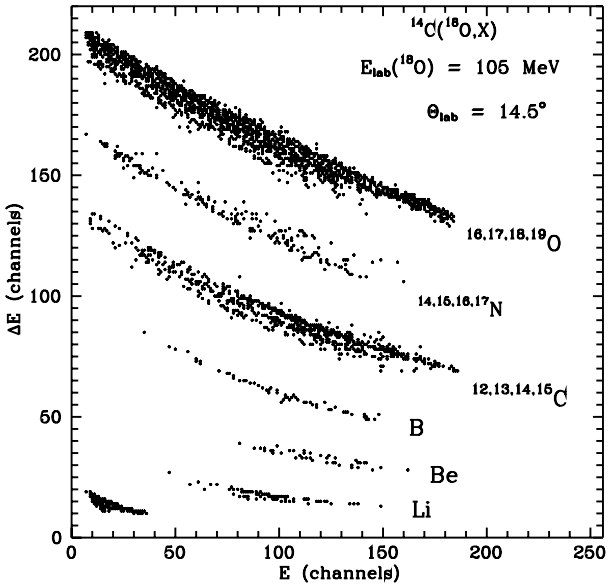

Fig. 1. Typical $\Delta E(E)$-spectra from the $^{14}\mathrm{C}(^{18}\mathrm{O},X)$ reactions at energy $E_{\mathrm{lab}}(^{18}\mathrm{O}) = 105\,\mathrm{MeV}$.

relative importance of the different scattering and particle transfer paths.

Typical residual energy (E) spectra of ^{18}O and ^{14}C from the reaction $^{14}\mathrm{C}(^{18}\mathrm{O},^{18}\mathrm{O})^{14}\mathrm{C}$ at the energy $E_{\mathrm{lab}}(^{18}\mathrm{O}) = 105\,\mathrm{MeV}$ after the subtraction of backgrounds by the procedure used in ref. [1] are shown in fig. 2a and fig. 2b, respectively.

The residual energy spectra were fitted by the sums of Gauss symmetric functions (curves in fig. 2a and fig. 2b)

$$N(E) = \sum_i N_i \exp\left(-0.5\frac{(E-E_i)^2}{h_i^2}\right) \qquad (1)$$

by fixing the E_i positions of the peaks to the corresponding level kinetic energies and using the $h_i = h$ width of the elastic-scattering peak for all other peaks, except naturally broad levels.

The fitting procedure provided the areas under the well-resolved and poorly-resolved peaks with errors of about 20–30% and 30–40%, respectively.

The areas under the peaks of the residual ^{18}O and ^{14}C spectra were used for the calculation of angular distributions at the angles $\theta_{\mathrm{c.m.}}(^{18}\mathrm{O})$ and $\theta_{\mathrm{c.m.}}(^{18}\mathrm{O}) = 180^\circ - \theta_{\mathrm{c.m.}}(^{14}\mathrm{C})$, respectively.

The angular distribution of the elastic scattering was normalized to the optical model (OM) cross-section at small angles where it is relatively independent of parameters. The normalization error was smaller than 15%.

The same factor was used to normalize the angular distributions for both elastic- and inelastic-scattering data at the forward and backward angles.

In fig. 3, the measured distribution of the $^{14}\mathrm{C} + ^{18}\mathrm{O}$ elastic scattering at the energy $E_{\mathrm{lab}}(^{18}\mathrm{O}) = 105\,\mathrm{MeV}$ (filled symbols) is compared a) with $^{12,13}\mathrm{C} + ^{18}\mathrm{O}$ elastic scattering at the same lab energy [1,2] (open symbols) and b) with the $^{14}\mathrm{C} + ^{16}\mathrm{O}$ elastic scattering at the energy $E_{\mathrm{lab}}(^{16}\mathrm{O}) = 132\,\mathrm{MeV}$ [3] (open symbols) as a function of the transferred momentum q_{t}. One can see that the main difference in the scatterings is that the large-angle cross-section for the $^{14}\mathrm{C} + ^{18}\mathrm{O}$ system is smaller than that for the other isotopes indicating the increased importance of other reaction channels for this system.

3 The data analysis

3.1 Calculation procedure

The $^{14}\mathrm{C} + ^{18}\mathrm{O}$ elastic- and inelastic-scattering data were analyzed within the OM and CRC method. Optical model potentials of Woods-Saxon (WS) type

$$\begin{aligned} U(r) = {} & V_0\left[1+\exp\left(\frac{r-R_V}{a_V}\right)\right]^{-1} \\ & + iW_S\left[1+\exp\left(\frac{r-R_{W_S}}{a_{W_S}}\right)\right]^{-1} \\ & + i4W_D\exp\left(\frac{r-R_{W_D}}{a_{W_D}}\right)\left[1+\exp\left(\frac{r-R_{W_D}}{a_{W_D}}\right)\right]^{-2}, \end{aligned} \qquad (2)$$

and Coulomb potentials of a uniform charged sphere

$$V_C(r) = \begin{cases} \frac{Z_P Z_T e^2}{2R_C}\left(3-\frac{r^2}{R_C^2}\right), & r \le R_C, \\ \frac{Z_P Z_T e^2}{r}, & r > R_C, \end{cases} \qquad (3)$$

with radius

$$R_i = r_i\left(A_P^{1/3} + A_T^{1/3}\right), \quad i = V, W, C \qquad (4)$$

were used in the OM and CRC calculations for the scattering of projectile ions (P) by target nuclei (T). The Coulomb parameter $r_i = 1.25\,\mathrm{fm}$ was used in all calculations.

Firstly, the $^{14}\mathrm{C} + ^{18}\mathrm{O}$ double-folding potential was calculated using charge distributions in these nuclei taken from ref. [4] and the simple double-folding model with the Reid M3Y NN-potential used in the code DFPOT [5,6]. As is known [7], this model provides for a realistic real part of a nucleus-nucleus potential in the peripheral region where nuclear processes take place mainly at beam energies $E_{\mathrm{lab}} < 10\,\mathrm{MeV/nucleon}$. For this reason, the $^{14}\mathrm{C} + ^{18}\mathrm{O}$ real part of the WS potential at $E_{\mathrm{lab}}(^{18}\mathrm{O}) = 105\,\mathrm{MeV}$ (5.8 MeV/nucleon) was fitted to the peripherical region of the double-folding potential and then it was used as the initial one in the OM fitting. Next, the optimal parameter set $X_{\mathrm{opt}} = \{V_0, r_V, a_V, W_S, r_{W_S}, a_{W_S}, W_D, r_{W_D}, a_{W_D}\}$ deduced from the OM fitting was then used as the initial one in the final CRC fitting procedure for elastic and inelastic scattering. It was found that the $^{14}\mathrm{C} + ^{18}\mathrm{O}$ potential parameters for the interaction of these nuclei in excited states are close to those for ground states.

In the CRC analysis, the $^{14}\mathrm{C} + ^{18}\mathrm{O}$ elastic and inelastic scattering for the transitions to the ground and excited

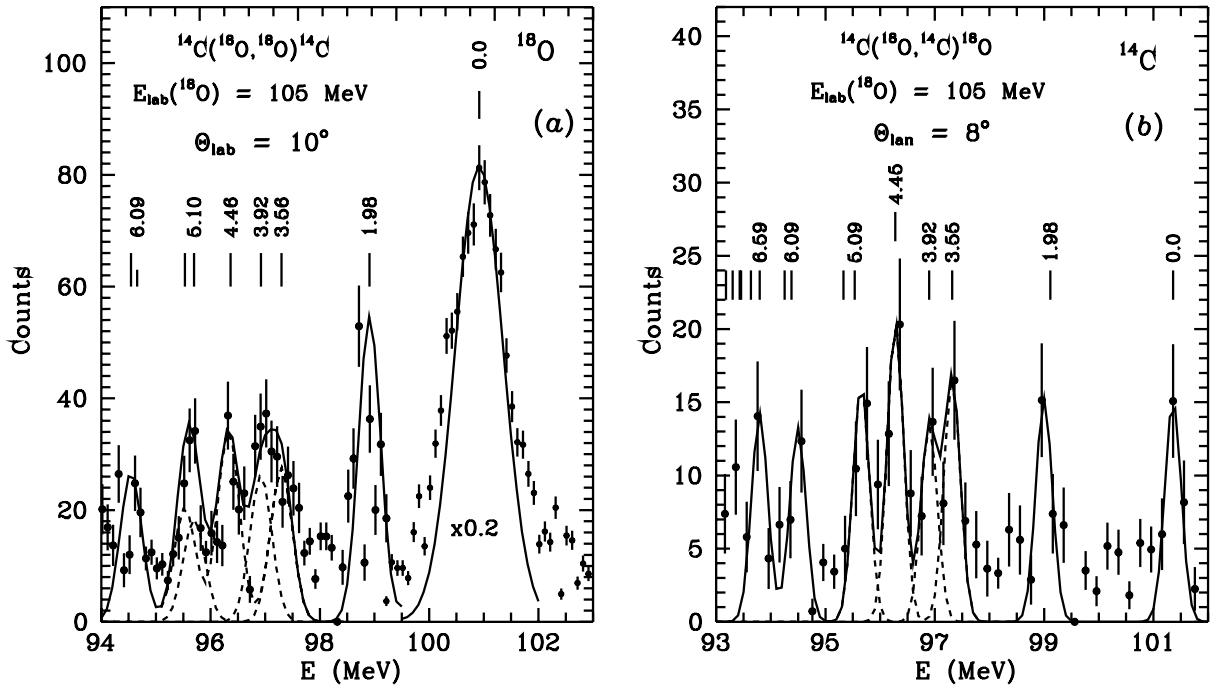

Fig. 2. Typical residual E-spectra of ^{18}O (a) and ^{14}C (b) from the reactions of $^{14}C(^{18}O, ^{18}O)^{14}C$ and $^{14}C(^{18}O, ^{14}C)^{18}O$ at the energy $E_{lab}(^{18}O) = 105\,MeV$ obtained by subtraction of backgrounds. The curves show the Gauss symmetric forms.

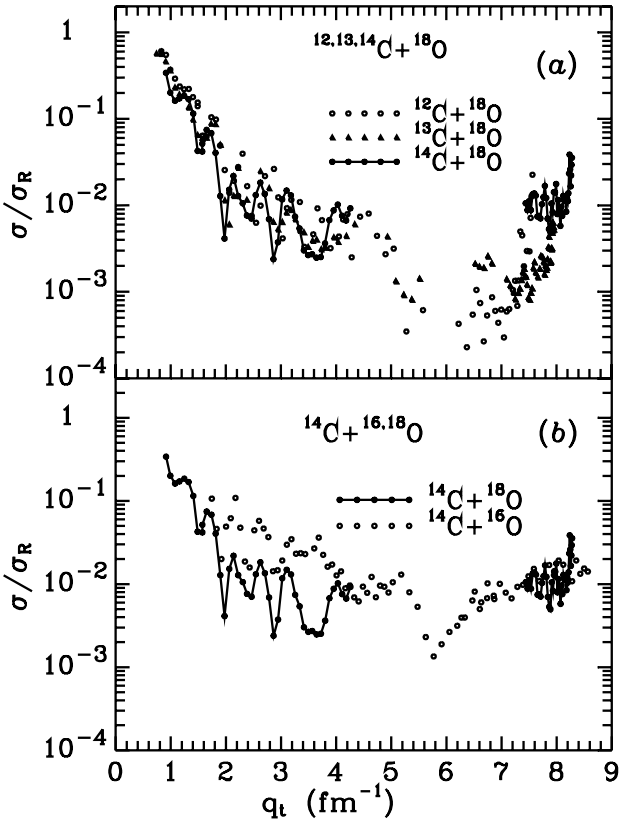

Fig. 3. Momentum transfer distributions q_t of $^{14}C + ^{18}O$ elastic scattering at the energy $E_{lab}(^{18}O) = 105\,MeV$ (filled symbols) *versus* $^{12,13}C + ^{18}O$ elastic scattering at the same lab energy [1,2] (open symbols) (a) and $^{14}C + ^{16}O$ elastic scattering at $E_{lab}(^{16}O) = 132\,MeV$ [3] (open symbols) (b).

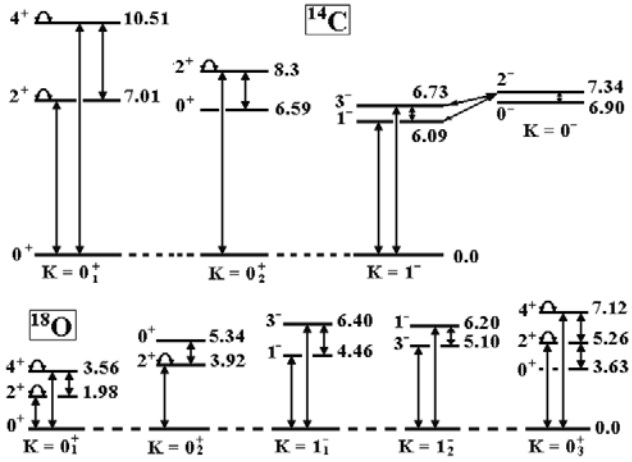

Fig. 4. Coupling schemes for the transitions to the excited states of ^{14}C and ^{18}O.

states of ^{14}C and ^{18}O as well as most important transfer reactions were included in the channels coupling scheme. Figure 4 shows the transitions to the excited states of ^{14}C and ^{18}O. The arcs show the quadrupole transitions for the spin reorientation processes of these nuclei in their excited states. These two-step processes give very small contributions to the direct transitions to these states but in some CRC codes they are included in the coupled-channels scheme. So far as such code is used in the present work, the reorientation transitions are shown in this figure. The diagrams of one- and two-step transfers, which contribute to the $^{14}C + ^{18}O$ and $^{14}C + ^{16}O$ scattering calculations, are presented in fig. 5.

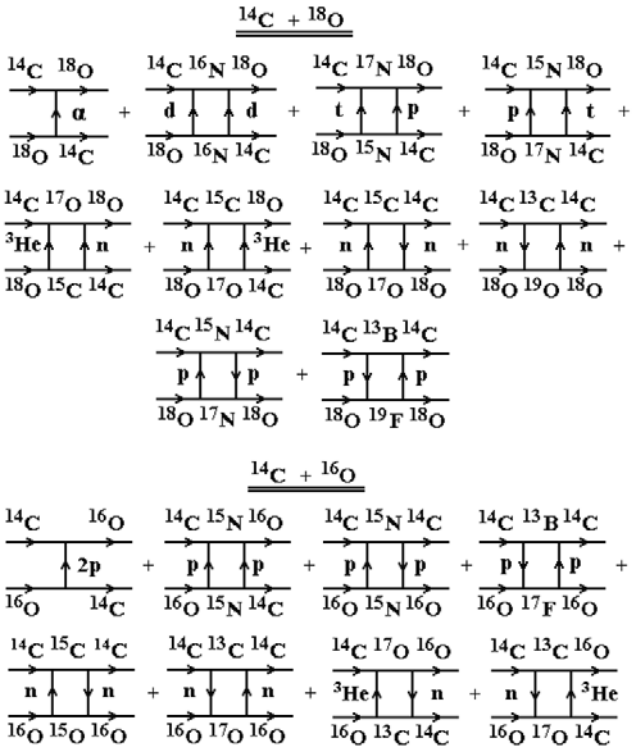

Fig. 5. Diagrams of one- and two-step transfers contributing to the $^{14}\mathrm{C} + ^{18}\mathrm{O}$ and $^{14}\mathrm{C} + ^{16}\mathrm{O}$ scattering calculations.

Table 1. Deformation parameters of ^{14}C and ^{18}O.

Nucleus	E_x (MeV)	J^π	λ	δ_λ (fm)	$\beta_\lambda^{(a)}$	Ref.
^{14}C	6.094	1^-	1	0.4	0.13	[8]
^{18}O	1.982	2^+	2	1.0	0.30	[9]
	3.555	4^+	4	1.0	0.30	[9]
	3.920	2^+	2	1.0	0.30	[9]
	4.456	1^-	1	1.0	0.30	[9]
	5.098	3^-	3	1.0	0.30	[9]
	5.255	2^+	2	1.0	0.30	[9]

(^{a}) In this work $\beta_\lambda = \delta_\lambda/R$, $R = 1.25A^{1/3}$.

We assume that the rotations of the deformed ^{14}C and ^{18}O nuclei as well as the vibrations dominate the low-energy excitations. The transitions to these states were calculated using the form factors

$$V_\lambda(r) = -\frac{\delta_\lambda}{\sqrt{4\pi}}\frac{\mathrm{d}U(r)}{\mathrm{d}r}\,, \tag{5}$$

where δ_λ is the length of the λ-multipole deformation. The deformation parameters for ^{14}C and ^{18}O used in the present CRC calculations are listed in table 1. These parameters were deduced previously from the analyses of the $^{14}\mathrm{C} + ^{11}\mathrm{B}$ and $^{7}\mathrm{Li} + ^{18}\mathrm{O}$ inelastic scatterings [8,9].

The spectroscopic amplitudes S_x of transferred clusters or nucleons x in the systems $A = C + x$ required for the CRC calculation of the transfer reactions were obtained within the translationally invariant shell model (TiSM) [11] using the code DESNA [12,13]. The amplitudes S_x are listed in table 2.

Table 2. Spectroscopic amplitudes S_x of x-clusters in the $A = C + x$ systems.

A	C	x	nL_j	S_x
^{13}C	^{12}B	p	$1P_{1/2}$	$0.283^{(a)}$
			$1P_{3/2}$	0.801
^{13}C	^{12}C	n	$1P_{1/2}$	0.601
^{14}C	^{13}B	p	$1P_{3/2}$	$1.695^{(a)}$
^{14}C	^{13}C	n	$1P_{1/2}$	$-1.094^{(a)}$
^{15}C	^{13}C	2n	$1P_1$	$0.802^{(a)}$
^{15}C	^{14}C	n	$2S_{1/2}$	-0.882
^{14}N	^{13}C	p	$1P_{1/2}$	0.461
			$1P_{3/2}$	$0.163^{(a)}$
^{15}N	^{13}C	d	$2S_1$	$0.248^{(a)}$
			$1D_1$	$0.444^{(a)}$
^{15}N	^{14}C	p	$1P_{1/2}$	-0.598
$^{16}\mathrm{N}^*_{3.52}$	^{14}C	d	$2D_2$	0.110
^{17}N	^{14}C	t	$1P_{1/2}$	0.466
^{16}O	^{12}C	α	$3S_0$	0.544
^{16}O	^{13}C	^{3}He	$2P_{1/2}$	$0.910^{(a)}$
^{16}O	^{14}C	2p	$2S_0$	$0.910^{(a)}$
^{16}O	^{14}N	d	$1D_1$	$1.400^{(a)}$
^{16}O	^{15}N	p	$1P_{1/2}$	$-1.461^{(a)}$
^{16}O	^{15}O	n	$1P_{1/2}$	$1.461^{(a)}$
^{17}O	^{13}C	α	$2D_2$	$0.191^{(a)}$
^{17}O	^{14}C	^{3}He	$2D_{5/2}$	-0.577
^{17}O	^{16}O	n	$1D_{5/2}$	$0.750^{(b)}$
^{18}O	^{14}C	α	$4S_0$	-0.802
$^{18}\mathrm{O}^*_{1.98}$	^{14}C	α	3D2	0.237
^{18}O	^{15}C	^{3}He	$3S_{1/2}$	$-0.903^{(a)}$
^{18}O	^{15}N	t	$2P_{1/2}$	$0.277^{(a)}$
^{18}O	$^{16}\mathrm{N}^*_{3.52}$	d	$2D_2$	-0.753
^{18}O	^{17}N	p	$1P_{1/2}$	$1.198^{(a)}$
$^{18}\mathrm{O}^*_{1.98}$	^{17}N	p	$1P_{3/2}$	$-1.198^{(a)}$
^{18}O	^{17}O	n	$1D_{5/2}$	$1.406^{(a)}$
$^{18}\mathrm{O}^*_{1.98}$	^{17}O	n	$2S_{1/2}$	$0.876^{(a)}$
^{19}O	^{18}O	n	$1D_{5/2}$	-0.882
^{19}O	$^{18}\mathrm{O}^*_{1.98}$	n	$2S_{1/2}$	0.889
^{17}F	^{16}O	p	$1D_{5/2}$	-0.500
^{19}F	^{18}O	p	$2S_{1/2}$	-0.707
^{19}F	$^{18}\mathrm{O}^*_{1.98}$	p	$1D_{5/2}$	1.315

(^{a}) $S_{\mathrm{FRESCO}} = (-1)^{J_C+j-J_A}S_x = -S_x$.

(^{b}) Experimental value taken from ref. [10].

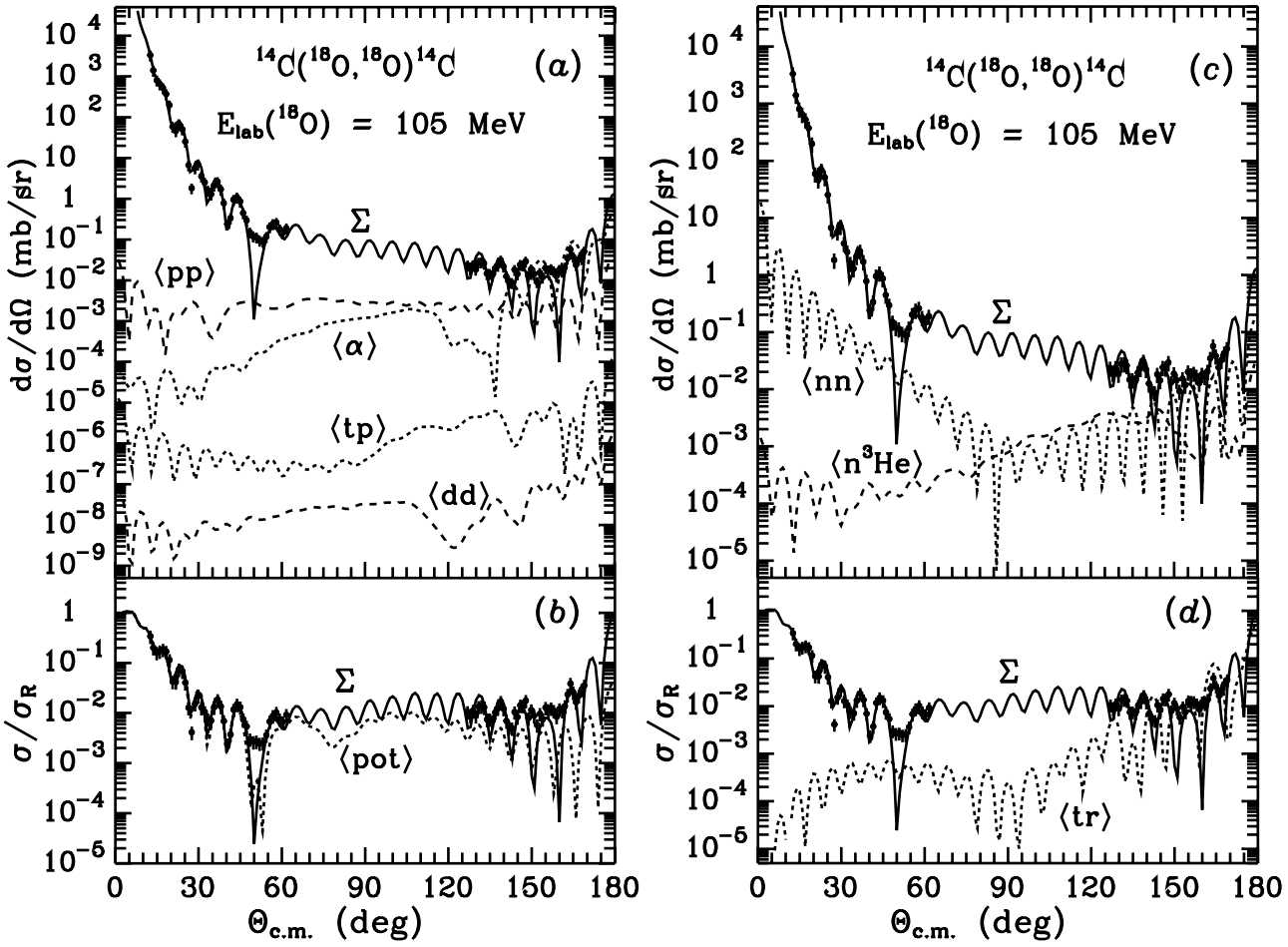

Fig. 6. Angular distributions of the $^{14}C + ^{18}O$ elastic scattering at the energy $E_{lab}(^{18}O) = 105$ MeV. The curves show the CRC calculations for the potential scattering (curve $\langle pot \rangle$) and transfers of x and $x + y, y + x$ nucleons or clusters (curves $\langle x \rangle$ and $\langle xy \rangle$, respectively). Curves $\langle tr \rangle$ and Σ show the coherent sums of all transfers and all processes, respectively.

The bound cluster wave function was calculated by fitting the Woods-Saxon potential parameter V to the x-cluster binding energy for

$$a = 0.65\,\text{fm} \qquad \text{and} \qquad r_V = 1.25A^{1/3}/(C^{1/3} + x^{1/3})\,\text{fm}.$$

The codes SPi-GENOA [14] and FRESCO [15] were used for the OM and CRC calculations, respectively.

3.2 Elastic scattering

The angular distributions of the measured $^{14}C + ^{18}O$ elastic scattering at the energy $E_{lab}(^{18}O) = 105$ MeV are shown in fig. 6. Due to different circumstances, the angular distributions for these elastic and inelastic scatterings were not measured at angles $\theta_{c.m.} = 70°$–$120°$ in the present experiment. In next experiments, it should be necessary to measure such data because they are important to decrease the potential parameter ambiguities in a fitting procedure [16].

In fig. 6 the curves show the CRC calculations with the $^{14}C + ^{18}O$ potential parameters deduced from the CRC fitting procedure. The three sets A_1, A_2 and A_3 of these parameters provided similar CRC descriptions of the data and their volume integrals per nucleon of J_V, J_{W_S}, and J_{W_D} are listed in table 3 where the potential parameters of $^{12}C + ^{18}O$ [1] (set B) and $^{13}C + ^{18}O$ [2] (set C) are given for a comparison. In fig. 6, the curves show the CRC calculations with A_3-parameters for the potential scattering (curves $\langle pot \rangle$) and transfers of x and $x + y$, $y + x$ nucleons and clusters (curves $\langle x \rangle$ and $\langle xy \rangle$, respectively), whose corresponding diagrams are shown in fig. 5. Both types of two-step transfers of x and y particles were summed coherently. Curves $\langle tr \rangle$ and Σ show the coherent sums of all transfers and all processes, respectively.

As fig. 6 shows, the potential scatterings (curves $\langle pot \rangle$) dominate at $\theta_{c.m.} < 120°$. The transfers are important only for the scatterings at larger angles. One can also see that numerous nucleon exchanges (curves $\langle nn \rangle$ and $\langle pp \rangle$) as well as α-, (n+^{3}He)- and (^{3}He+n)-transfers (curves $\langle \alpha \rangle$ and $\langle n^3He \rangle$, respectively) dominate at the larger angles.

Previously obtained potential parameter sets for the systems $^{12,13}C + ^{18}O$ at the same lab energy (sets B and C in table 3, respectively) $E_{lab}(^{18}O) = 105$ MeV were used in the $^{14}C + ^{18}O$ CRC calculations to determine the

Table 3. Parameters of the $^{12,13,14}C + {}^{18}O$ and $^{14}C + {}^{16}O$ potentials.

Systems	$E_{c.m.}$ (MeV)	V (MeV)	r_V (fm)	a_V (fm)	W_S (MeV)	r_{W_S} (fm)	a_{W_S} (fm)	W_D (MeV)	r_{W_D} (fm)	a_{W_D} (fm)	J_V, J_{W_S}, J_{W_D} (MeV · fm^3)	Ref., (Set)
$^{12}C + {}^{18}O$	42.0	259.3	0.820	0.680	14.9	1.200	0.450	1.00	1.400	0.350	421, 63, 3.9	[1], (B)
$^{13}C + {}^{18}O$	44.0	309.0	0.790	0.729	16.1	1.126	0.729	0.13	1.227	0.233	449, 59, 0.2	[2], (C)
$^{14}C + {}^{18}O$	45.9	264.1	0.789	0.747	6.1	1.225	0.284	4.47	1.188	0.724	371, 24, 24.2	(A_1)
		264.1	0.789	0.747	8.0	1.312	0.756	2.75	1.082	0.290	371, 43, 4.8	(A_2)
		264.1	0.789	0.747	9.7	1.243	0.747				371, 45, 0.0	(A_3)
$^{14}C + {}^{16}O$	61.6	290.0	0.780	0.800	12.0	1.250	0.478	2.50	1.222	0.489	440, 56, 10.2	
		361.0	0.577	1.031	11.4	1.330	0.466				360, 63, 0.0	[3] (D)
	131.1	290.0	0.780	0.800	20.0	1.250	0.678	2.50	1.222	0.489	440, 98, 10.2	

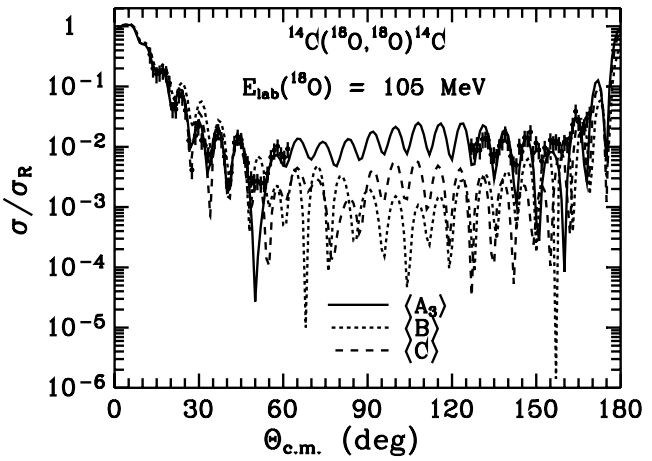

Fig. 7. Comparison of the CRC calculations with parameter sets of A_3, B and C (table 3) for the $^{14}C + {}^{18}O$ elastic scattering at energy $E_{lab}(^{18}O) = 105$ MeV.

isotopic differences in the elastic scatterings. These CRC calculations are shown in fig. 7 where it is seen that large differences in the CRC angular distributions occur at the middle angles where the differences in the absorptive potentials play an important role.

To compare the $^{14}C + {}^{16,18}O$ potentials, the data of the $^{14}C + {}^{16}O$ elastic scattering at the energies $E_{lab}(^{16}O) =$ 132 and 281 MeV ($E_{c.m.} = 61.6$ and 131.13 MeV, respectively) [3] were also studied by a CRC analysis. The $^{14}C + {}^{16}O$ elastic scattering and corresponding transfer reaction diagrams included in the coupled-channels scheme are shown in fig. 5. The $^{14}C + {}^{16}O$ potential parameters deduced from the calculations and taken from ref. [3] (set D) are listed in table 3. The $^{14}C + {}^{16}O$ elastic-scattering data and CRC calculations for the various processes contributing to them are shown in fig. 8.

As this figure shows, the potential scattering dominates (curves $\langle$pot$\rangle$) at $\theta_{c.m.} < 100°$ and $\theta_{c.m.} < 60°$ for the energies 132 MeV and 281 MeV, respectively. The 2p-cluster transfer (curves $\langle$2p$\rangle$) dominates at large angles and the proton exchange (curves $\langle$pp$\rangle$) is important at middle angles. The curves $\langle$tr$\rangle$ and Σ show the CRC calculations for the coherent sums of all transfers and all processes, respectively.

Figure 8 also displays the CRC angular distributions for the sums of all processes calculated with the A_3-parameters of the $^{14}C + {}^{18}O$ potential (curves $\langle{}^{18}O\rangle$). As one can see, the CRC calculations do not describe the $^{14}C + {}^{16}O$ elastic-scattering data.

In fig. 9, the $^{14}C + {}^{18}O$ potential for the parameter sets A_1, A_2 and A_3 as well as the real part of this potential and of the folding potential are compared. As one can see, the imaginary parts are different in the interior radial region but they are very similar in the region where the nucleus-nucleus interaction occurs. Therefore, these potentials support those that have been found through the CRC analysis.

The $^{12}C + {}^{18}O$ [1], $^{13}C + {}^{18}O$ [2] and $^{14}C + {}^{18}O$ potentials are compared in figs. 10a and b to those of the $^{14}C + {}^{18}O$ and $^{14}C + {}^{16}O$ systems. As can be seen, the real parts of these potentials are close and only the imaginary parts differ. Figure 10b shows also the real part of the $^{14}C + {}^{16}O$ potential obtained from the OM analysis of the data at $E_{lab}(^{16}O) = 132$ MeV in ref. [3] (set D in table 3). One can see that the real parts of the potential for both parameter sets are close in the interior region up to 8 fm where the nuclear processes play a principal role. As can be seen in table 3, both sets of parameters for the imaginary part of this potential are also close.

3.3 Inelastic scattering

The angular distributions of the $^{14}C + {}^{18}O$ inelastic scattering measured simultaneously with the elastic scattering at $E_{lab}(^{18}O) = 105$ MeV are shown in figs. 11–13. They are all strongly forward peaked indicating strong inelastic scattering in these systems.

Figure 11 shows the angular distribution for the transition to the 1.982 MeV (2^+) state of ^{18}O. Note that the large-angle cross-section is of similar magnitude to that of the elastic scattering providing further evidence

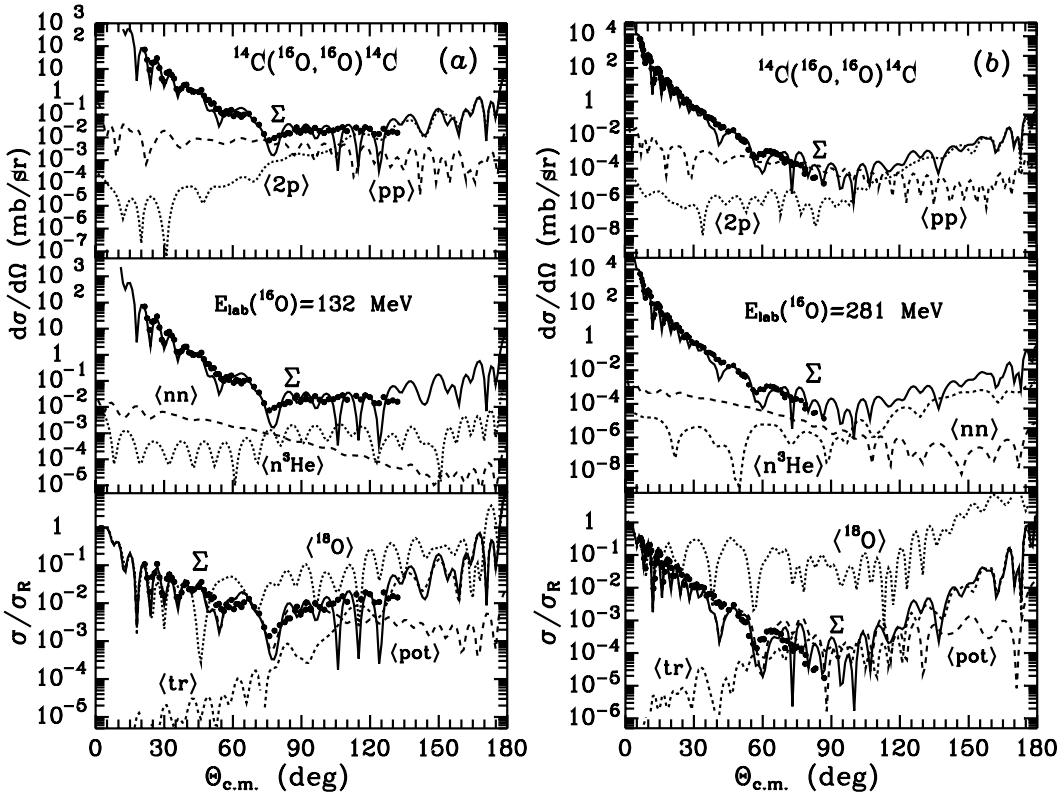

Fig. 8. Angular distributions of the $^{14}C + {}^{16}O$ elastic scattering at the energy $E_{lab}(^{16}O) = 132\,MeV$ (a) and 281 MeV (b) [3]. The curves show the CRC calculations for the potential scattering (curve $\langle pot \rangle$) and transfers of 2p, n + n, p + p and n + ^{3}He, ^{3}He + n nucleons or clusters (curves $\langle 2p \rangle$, $\langle nn \rangle$, $\langle pp \rangle$ and $\langle n^3He \rangle$), respectively. Curves $\langle tr \rangle$ and Σ show the coherent sums of all transfers and all processes, respectively.

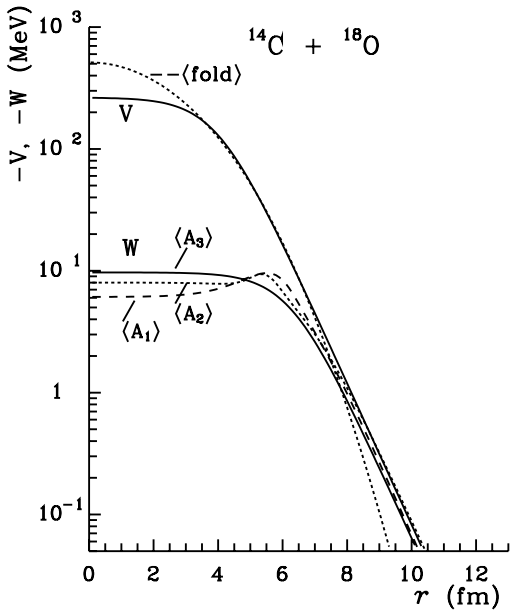

Fig. 9. Comparison of the real part of the $^{14}C + {}^{18}O$ potential (curve $\langle V \rangle$) with the corresponding double-folding potential (curve $\langle fold \rangle$) and three $^{14}C + {}^{18}O$ potentials corresponding to the parameter sets A_1, A_2 and A_3 (table 3, curves $\langle A_1 \rangle$, $\langle A_2 \rangle$ and $\langle A_3 \rangle$, respectively).

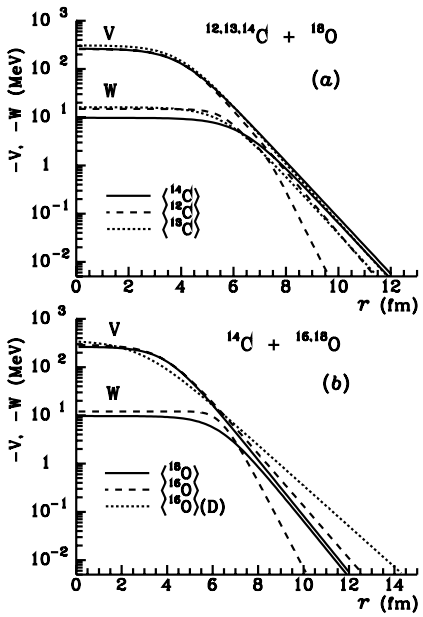

Fig. 10. Comparison of the $^{12,13,14}C + {}^{18}O$ potentials for the energy $E_{lab}(^{18}O) = 105\,MeV$ (curves $\langle {}^{12}C \rangle$, $\langle {}^{13}C \rangle$ and $\langle {}^{14}C \rangle$, respectively) (a) and $^{14}C + {}^{16,18}O$ potentials for $E_{lab}(^{18}O) = 105\,MeV$ (solid curves $\langle {}^{18}O \rangle$) and $E_{lab}(^{16}O) = 132\,MeV$ (dashed curves $\langle {}^{16}O \rangle$ and $\langle {}^{16}O \rangle$ (D)) (b).

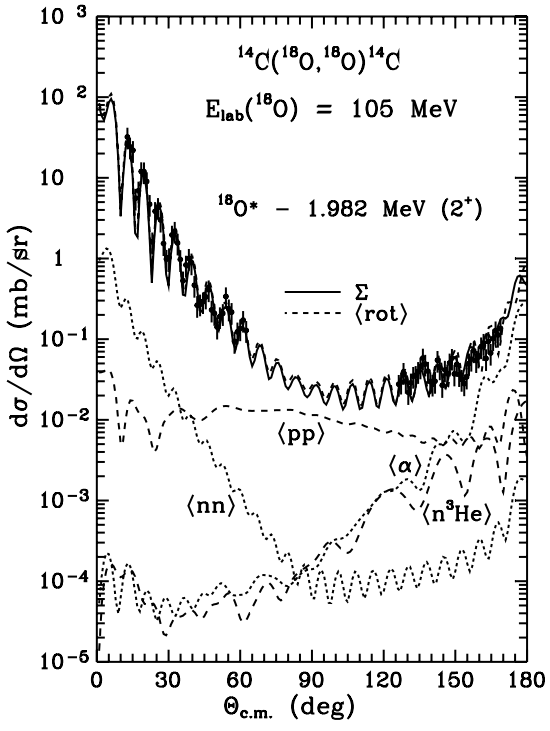

Fig. 11. Angular distribution of the $^{14}C + {}^{18}O$ inelastic scattering at $E_{lab}(^{18}O) = 105\,MeV$ for the transition to the 1.982 MeV (2^+) state of ^{18}O. The curves show the CRC calculations for rotational transition (curve $\langle rot \rangle$) and transfers of nucleons and clusters (other curves).

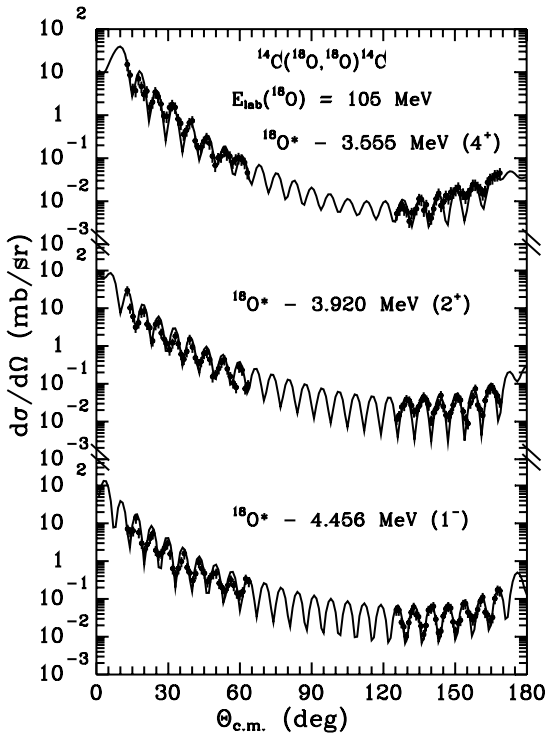

Fig. 12. Angular distributions of the $^{14}C + {}^{18}O$ inelastic scattering at $E_{lab}(^{18}O) = 105\,MeV$ for the transitions to the excited states of ^{18}O. The curves show the CRC calculations assuming collective transitions.

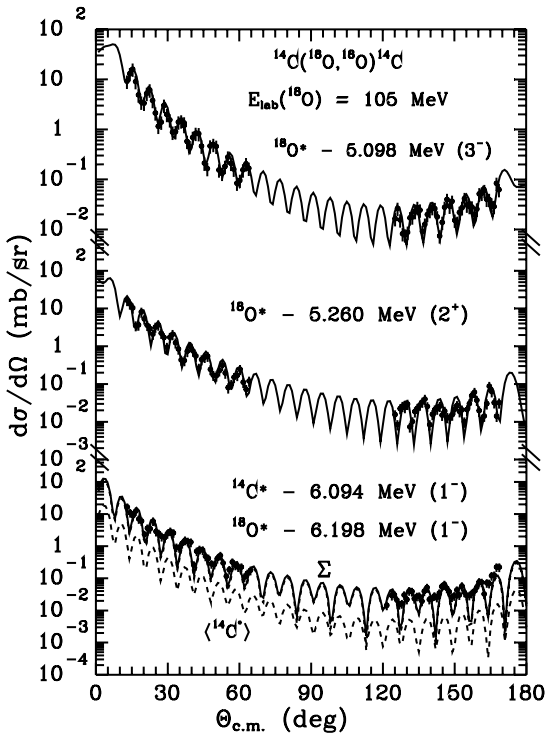

Fig. 13. The same as in fig. 12 but for other transitions.

for the need for CRC calculations to describe the large-angle data. The curves show the CRC calculations for a rotational transition (curve $\langle rot \rangle$) as well as for the nucleon exchanges (curves $\langle nn \rangle$ and $\langle pp \rangle$), α-particle and ($n + {}^3He$), ($^3He + n$) transfers (curves $\langle \alpha \rangle$ and $\langle n^3He \rangle$), respectively. As one can see, the rotational transition dominates throughout the whole angular range and, in fact, it does the same for the other collective transitions to the excited states of ^{14}C and ^{18}O shown in figs. 12 and 13.

In fig. 11, the curve Σ shows the CRC calculations for the coherent sum of all processes. In figs. 12 and 13, the curves are only for the CRC calculations for the collective transitions to the excited states of ^{14}C and ^{18}O. Such transitions to the 6.094 MeV (^{14}C) + 6.198 MeV (^{18}O) unresolved in the experiment are shown in fig. 13 with dashed curves and their incoherent sum is presented by curve Σ. One can see that the CRC calculations for collective transitions describe satisfactorily the $^{14}C + {}^{18}O$ inelastic scattering.

4 Summary and conclusions

For the first time, angular-distribution data for $^{14}C + {}^{18}O$ elastic and inelastic scattering at $E_{lab}(^{18}O) = 105\,MeV$ are reported. These data were analyzed with the optical model and the coupled-reaction-channels methods. The transitions to the excited states were calculated using the rotational and vibrational models. Elastic and inelastic channels as well as strong particle transfers were included in the coupling scheme.

In the $^{14}C + ^{18}O$ elastic channel, the potential scattering dominate at angles $\theta_{c.m.} < 120°$. One- and two-step transfers give substantial contributions to the elastic scattering only at backward angles where the cross-section is of the same magnitude as that for the inelastic scattering. The collective transitions to excited states in ^{14}C and ^{18}O dominate the scattering over the full anglular region.

The CRC analysis of the $^{14}C + ^{16}O$ elastic-scattering data at $E_{lab}(^{18}O) = 132\,MeV$ and $281\,MeV$ [3] shows that the potential scattering dominates at angles $\theta_{c.m.} < 90°$ while 2p-cluster transfers dominate at large angles at both energies. The $^{14}C + ^{16,18}O$ potentials differ strongly only in their imaginary parts which are similar to those found in the $^{12,13,14}C + ^{18}O$ potentials.

The calculated $^{14}C + ^{18}O$ real double-folding potential is close to that found from the CRC analysis in the principal radial region of the nucleus-nucleus interaction giving support to the CRC analyses carried out in the present and previous works.

We thank Prof. A. Sobiczewski, Prof. J. Jastrzêbski and Dr. A.G. Artukh for their interest in this work.

References

1. A.T. Rudchik, Yu.O. Shyrma, K.W. Kemper *et al.*, Eur. Phys. J. A **44**, 221 (2010).
2. A.T. Rudchik, Yu.O. Shyrma, K.W. Kemper *et al.*, Nucl. Phys. A **852**, 1 (2011).
3. A.S. Dem'yanova, Yu.A. Glukhov, W. Trzaska *et al.*, Bull. Russ. Acad. Sci. Phys. **67**, 83 (2003).
4. H. De Vries, C.W. De Jager, C. De Vries, At. Data Nucl. Data Tables **36**, 495 (1987).
5. J. Cook, Comput. Phys. Commun. **25**, 125 (1982).
6. J. Cook, Comput. Phys. Commun. **35**, 775 (1984).
7. Dao T. Khoa, G.R. Satchler, Nucl. Phys. A **668**, 3 (2000).
8. S.Yu. Mezhevych, A.T. Rudchik, K. Rusek *et al.*, Nucl. Phys. A **753**, 13 (2005).
9. A.A. Rudchik, A.T. Rudchik, S. Kliczewski *et al.*, Nucl. Phys. A **785**, 293 (2007).
10. Jenny Lee, J.A. Tostevin, B.A. Brown *et al.*, Phys. Rev. C **73**, 044608 (2006).
11. Yu.F. Smirnov, Yu.M. Tchuvil'sky, Phys. Rev. C **15**, 84 (1977).
12. A.T. Rudchik, Yu.M. Tchuvil'sky, *The code DESNA*, The Kyiv Institute for Nuclear Research, Report no. KiYai-82-12 (1982).
13. A.T. Rudchik, Yu.M. Tchuvil'sky, Ukr. Fiz. Zh. **30**, 819 (1985).
14. B.S. Nilsson, *SPi-GENOA: An Optical Model Search Code*, Niels Bohr Institute Report (1976).
15. I.J. Thompson, Comput. Phys. Rep. **7**, 167 (1988).
16. T.I. Belyaeva, A.N. Danilov, A.S. Demyanova *et al.*, Phys. Rev. C **82**, 054618 (2010).